The structural and magnetic features of perovskite oxides La1−xSrxMnO3+δ (x = 0.05, 0.10, 0.20) depending on the strontium doping content and heat treatment

Diana Pchelina, Vera Sedykh, Nataliya Chistyakova, Vyacheslav Rusakov, Yulia Alekhina, Alexey Tselebrovskiy, Bernard Fraisse, Lorenzo Stievano, Moulay Tahar Sougrati

The structural and magnetic features of perovskite oxides $La_{1-x}Sr_xMnO_{3+\delta}$ (x = 0.05, 0.10, 0.20) depending on the strontium doping content and heat treatment

Diana I. Pchelina[a*], Vera D. Sedykh[b], Nataliya I. Chistyakova[a], Vyacheslav S. Rusakov[a], Yulia A. Alekhina[a], Alexey N. Tselebrovskiy[a], Bernard Fraisse[c], Lorenzo Stievano[c*] and Moulay Tahar Sougrati[c]

[a]Lomonosov Moscow State University, Moscow, 119991 Russia

[b]Institute of Solid State Physics, Russian Academy of Sciences, Chernogolovka, 142432 Russia

[c]ICGM, Univ. Montpellier, CNRS, ENSCM, Montpellier, France

*Corresponding author at:

Lomonosov Moscow State University, GSP-1, Leninskie Gory, Moscow, 119991, Russia

Tel. +34 60006 33 88

E-mail: di.pchelina@physics.msu.ru

ICGM, Université Montpellier, CNRS, Place Eugène Bataillon, Montpellier, 34095, France

Tel. +33 (0) 4 67 14 93 50

E-mail: lorenzo.stievano@umontpellier.fr

Abstract

Sr-doped ($0<x<0.2$) ceramic samples of the lanthanum manganite oxides were obtained via sol-gel method to investigate the influence of doping on structural, magnetic end electronic responses, and their correlations. Synthesized samples of non-stoichiometric compositions are rhombohedral single-phase. After annealing the formation of a phase-separated system as a mixture of orthorhombic phases was found. The *R-3c* and *PnmaI, PnmaII** and *PnmaII* phases have been studied using Mössbauer spectroscopy, XRD, SEM analysis and magnetic measurements. The magnetic temperature-concentration phase diagram of $La_{1-x}Sr_xMnO_{3+\delta}$ (x = 0.05, 0.10, 0.20) was obtained.

The Jahn-Teller effect or the orbital order breaking, as well as the competition between Mn^{3+}–O^{2-}—Mn^{4+} double- and Mn^{3+}–O^{2-}–Mn^{3+} superexchange interaction was demonstrated under the effect of cation doping compound and interstitial oxygen value (δ). The relaxation character of the Mössbauer spectra and the type of magnetization dependences revealed nanosized magnetic clusters with fluctuation of their magnetic moment in all perovskite phases. Results are interpreted in terms of matrix – clusters: regions of sample with ferromagnetic type of ordering (cluster) exist in antiferromagnetically or ferromagnetically (with different exchange parameter) ordered matrix. Exchange interaction frustrations of the cluster with the matrix can lead to relaxation behavior of the magnetic moment of the cluster. The clusters size vary from about 3.9 to 5.7 nm. All samples are characterized by the presence of particles agglometates with a typical size about 0.4-0.8 μm; for annealed samples additional non-conducting regions with 80-220 nm in size were found. It is shown that the annealing time significantly affects the production of materials with determined properties and be useful in the applied field in technological processes.

Keywords: perovskites**,** doped lanthanum manganites, Mössbauer spectroscopy, phase separation, magnetic properties, superparamagnetism.

1. Introduction

Alkaline-earth metal-doped perovskites $La_{1-x}A_xMnO_{3+\delta}$ (A = Ca^{2+}, Sr^{2+} or Ba^{2+}) are of great interest in the physics of strongly correlated systems with considerable fundamental and technological interest. They belong to the class of mixed valence manganites ceramics [1,2]. These materials have wide range of unique properties like colossal magneto-resistance (CMR) [3,4], high electrical conductivity [5], electrocatalytic properties [6], etc. Manganite materials are prospective in technological applications such as elements for solid oxide fuel cells [7], magnetic refrigeration [8], information recording devices and solid-state drives [9], the creation of digital microcircuits with magneto-optical converters on their basis [10], creation of temperature stabilizing (TS) coatings [11] and for magnetic hyperthermia [12,13].

Mn^{3+}/Mn^{4+} ratio depends on the cations doping and δ value. In these compounds, there is a strong correlation between the lattice, magnetic and electronic subsystems; therefore, changes in the structure lead to significant changes in the physical properties (transport, magnetic). Varying the type and the content of the doping element leads to significant changes: the system passes through a chain of phase transitions with various types of ordering.

The fact that the starting compound $LaMnO_3$ with Mn at single valence state behaves as antiferromagnetic insulator at low temperatures, could be explained by super-exchange mechanism existing between two Mn ions with same valence state based on Kanamori-Goodenough rules [14]. It was found that partial oxidation of Mn^{3+} to Mn^{4+} and formation of oxygen vacancies are observed when La is replaced by a divalent element A [15,16]. $La_{1-x}A_xMnO_3$ with $0.10 \leq x \leq 0.21$ becomes a ferromagnetic insulator, and with $0.21 \leq x \leq 0.40$ - ferromagnetic metal [17]. Ferromagnetic behavior was explained by double exchange mechanism existing between two Mn ions with different valence states [3,14]. When $x > 0.5$ the system again becomes an antiferromagnetic insulator [18].

Different synthesis conditions implement to obtain several structural modifications of $La_{1-x}A_xMnO_{3+\delta}$: the rhombohedral *R-3c* phase, monoclinic $P112_1/a$ phase, and three orthorhombic *PnmaI* (O), *PnmaII* (O′), *PnmaII** (O" or O*) phases [19–25]. The presence of *PnmaII** phase, like an intermediate phase in $LaMnO_{3+\delta}$ phase transition *PnmaI* → *PnmaII** → *PnmaII*, was confirmed by both X-ray diffraction and Mössbauer spectroscopy [25].

Doped lanthanum manganites have distorted perovskite structure which primarily depends on the nature and concentration of the dopant. Mn^{3+} - Jahn-Teller ion degenerates orbital state of electrons. Due to the Jahn-Teller effect, orbital ordering occurs (the electronic subsystem has short and long ordered bonds). Orbital ordering leads to severe lattice distortion. As a result, a strong correlation arises between the lattice and electronic subsystems [26]. Thus, Jahn-Teller effect leads to a strongly distorted lattice and a decrease in the lattice symmetry (*PnmaII* phase). Mn^{4+} is not a Jahn-Teller ion, its appearance leads to the destruction of orbital ordering and the transition to a more symmetrical environment (transition to the highly symmetric phase *PnmaI* through the intermediate *PnmaII**). The most outstanding structural and magnetic transitions are observed in the range of doping concentrations at x <0.20 [27]. However, such studies are very rare in the literature. Our previous investigations of stoichiometric $La_{1-x}Sr_xMnO_3$ containing low amounts of dopants, carried out at room temperature, revealed structural phase separation correlated with the Jahn-Teller effect [28]. For $La_{1-x}Ca_xMnO_{3+\delta}$ low temperature investigations revealed new properties of these manganite phases and cluster formation[29].

The present work is focused on the study of strontium-doped lanthanum manganite $La_{1-x}Sr_xMnO_{3+\delta}$ (x = 0.05, 0.10, 0.20), synthesized by the sol-gel method. Compared to previous studies [28], we paid attention to the low-temperature region (particularly from 5 K), using a novel Mössbauer methodologies with theoretical modeling and calculations, the magnetic temperature-dependent approaches, and electronic comparison. This comprehensive study of $La_{1-x}Sr_xMnO_{3+\delta}$ in wide temperature range allowed to reveal the structural and magnetic phase transitions, effect of doping on structural, hyperfine and magnetic properties were analyzed. The correlations between Mössbauer parameters and magnetic response were established. The duration of annealing influence on the features of the structure, changes in the phase composition, as well as the thermal stability were also investigated.

2. Material and methods

Non-stoichiometric $La_{1-x}Sr_xMnO_{3+\delta}$ (x = 0.05, 0.10, 0.20), labelled LS5-NS, LS10-NS, LS20-NS respectively, were prepared by the sol-gel method in the corresponding proportions [28]. LS5-NS sample was annealed for 8 hours to obtain transient state (LS5*). Stoichiometric $La_{1-x}Sr_xMnO_3$ (LS5-S, LS10-S, LS20-S) series was obtained by annealing under vacuum (10^{-3} Torr) at 650 °C for 10-15 hours [28].

2% of isotopically-enriched ^{57}Fe is added in all samples ($La_{1-x}Sr_xMn_{0.98}{}^{57}Fe_{0.02}O_{3+\delta}$) for Mössbauer investigations using a ^{57}Co (Rh) source on an MS-1104Em spectrometer at T = 300 K and 80 K and a WissEl spectrometer equipped with a Janis SHI-850 cryostat for analysis at T = 80 K and 5 K. It was described in [30] that ^{57}Fe replace Mn^{3+} in the crystal structure as Fe^{3+}, and does not introduce any distortion in the lattice (since the ionic radii of Fe^{3+} and Mn^{3+} are very similar and according to XRD the lattice parameters are not modified [30,31]. The spectra were processed using the SpectrRelax program [32].

Magnetostatic measurements were investigated by LakeShore 7407 vibrating sample magnetometer in the 100-400 K temperature range in fields up to 1280 kA/m (16 kOe). The temperature dependence of the magnetization in ZFC-FC mode (heating in a nonzero field after cooling in a zero magnetic field (ZFC - Zero-Field Cooled) and cooling in a non-zero field (FC - Field Cooling)) was obtained in an external magnetic field of 2.4 kA/m (30 Oe) and 8 kA/m (100 Oe) and in the temperature range of 100-400 K.

Alternating current (AC) magnetic susceptibility was investigated using AGICO Kappabridges MFK1-A instrument in the temperature range of 70-275 K in 200 A/m (2.5 Oe). The antiferromagnet-paramagnet phase transition temperature - the Neel temperature– was defined as an inflection point on temperature curve. This point is equivalent to a point of a minimum of derivative on temperature min($d\chi/dT$). Curie-Weiss temperature T_C was determined by linear extrapolation from the $1/\chi$ vs. temperature experimental plot [33].

Scanning electron microscopy investigations were carried out using Carl Zeiss Supra 40 at the Educational and Methodological Center for Lithography and Microscopy, Lomonosov Moscow State University. The processing of the obtained images (mean value and standard deviation of investigated samples size distribution, calculated from SEM images) made in the program ImageJ.

3. Results and discussion

3.1. Crystal features and SEM analysis

The dependence of the Mn^{4+} ions concentration on the Sr content in $La_{1-x}^{3+}Sr_{x}^{2+}Mn_{y}^{4+}Mn_{1-y}^{3+}O_{3+\delta}^{2-}$ using the data of iodometric titration [31] and electroneutrality was plotted in Fig.1. The yellow circles indicate the coordinates of the states corresponding to the *R-3c* phase, the green circles – the orthorhombic phases (sp. gr. *Pnma*), the semitransparent circles indicate the hypothetical coordinates of the states for the phases of initial LS5-NS, LS10-NS, LS20-NS samples and LS5* sample. Blue triangles indicate data taken from the literature [19,20,34–37]. The areas of Mn^{4+} ions concentration within which phases (*R-3c, PnmaI, PnmaII*) for $LaMnO_3$ realized are highlighted from [38,39]. Doping, in general, shifts the boundaries of the concentration range of certain structural modification (phases) existence, however, it is clear that in edge cases the coordinates of the states for each of the phases fit under the boundary conditions. For non-stoichiometric samples the δ value decreases with Sr concentration increasing. Apparently, there is also a decrease in the concentration of Mn^{4+} ions (dashed circles indicate possible positions for samples LS5-NS and LS10-NS on the graph), to a critical value equal to 0.2, at which the oxygen stoichiometry δ=0 is reached (LS20-NS and LS20-S). For stoichiometric samples the amount of Mn^{4+} ions equals to x, and changes linearly.

The XRD lattice parameters, volume of unit cell of all investigated samples are given in Table 1 [28]. The results for the synthesized single-phase samples LMS-NS show rhombohedral symmetry – *R-3c* space group for all samples. After vacuum annealing in LS5-S and LS10-S samples orthorhombic phases of the *Pnma* space group were detected. The *PnmaI* phase is considered to be higher symmetric than *PnmaII*. Annealing in vacuum for 8 hours leads to structural transition from *R-3c* phase into *PnmaI* (LS5* sample), which, upon further 10-15 hours of vacuum annealing, transforms into *PnmaII** (LS5-S and LS10-S samples). The distorted structures are transformed from orthorhombic to rhombohedral with increasing Sr concentration in a mixture of stoichiometric low-doping lanthanum manganites since their patterns are very close to each other. There are no changes for the case of LS20-S sample compared to LS20-NS.

The unit cell volume after vacuum annealing changes by about 30% that indicates the removal of interstitial oxygen. The slight differences in unit cell parameters are caused by difference in the ionic

radii. Ionic radius of Sr is approximately the same as for La, this means that aliovalent doping Sr^{2+} for La^{3+} does not add any distortions to the lattice, accompanied by partial Mn oxidation to Mn^{4+} (Mn^{3+} = 0.645 Å, Mn^{4+} = 0.53 Å) and decreasing in Mn-O-Mn bond angle. Aliovalent doping is also attributed to the appearance of oxygen holes, according to electrical properties and interactions, associated with the transition of a delocalized electron from the p-level of O to the d-level of Mn (Mn^{3+} in the high-spin configuration) [15,16,40].

XRD analysis does not reveal the presence of small particles – the lines are narrow. For average particle size estimation scanning electron microscopic investigations were carried out as shown in Fig.2. All images are obtained in secondary electrons. Samples are characterized by the presence of particle agglomerates with the minimum size about 100 nm, while their typical size is about 0.4-0.8 μm (Table 2). It can be noted that for LS5-S sample, the formation of agglomerates dense packing is observed – the particles are located close to each other. With an increase in Sr concentration to x=0.20 all particles are far from each other. The size of the agglomerates in both LMS-NS and LMS-S samples is practically the same; however, with an increase in Sr concentration, a decrease in the size is observed.

It should be noted that all samples exhibit high crystallinity “aspect” at high magnifications. The absence of compositional contrast in the images indicates a similar elemental composition in the samples. Samples of non-stoichiometric composition are characterized by the presence of a conducting phase, in contrast to a sample of stoichiometric composition, where light and dark areas can be distinguished. The images for the stoichiometric sample show “charging effects” (bright white areas), demonstrate the presence of non-conductive phases. The characteristic size of such white "non-conductive" areas is about 80-220 nm and such observations may indicate the presence of phase separation.

3.2. ^{57}Fe Mössbauer spectroscopy analysis

The Mössbauer spectra of doped lanthanum manganites of non-stoichiometric composition at 300 K and 80 K are presented in Fig. 3, obtained parameters phase are given in Table 3. The LS5-NS [41] and LS10-NS spectra at 300 K were fitted using the distribution of quadrupole splitting. The LS20-NS spectrum was also fitted using quadrupole splitting distribution with adding the relaxation type sextet with 55 kOe hyperfine magnetic field, the intensity of which is 30.6 ± 2.4%.

Each doublet corresponds to the *R-3c* phase with the parameters characterized trivalent iron atoms in a high-spin state in an octahedral oxygen environment. The δ_{max} values are approximately the same for all three experimental spectra. The Δ_{max} values corresponding to the rhombohedral phase decrease with an increase in Sr content, the minimum value reached for LS20-NS (Δ_{max} = 0.230 mm/s), is due to the decrease of interstitial oxygen value in accordance with Fig. 1. The distribution of full width at middle height (FWHM) becomes smaller with Sr content increase, indicating an increase in the symmetry of the environment of Fe^{57} ions and a decrease in the nearest environment distortion. Such changes lead to a decrease in the electric field gradient in the region where the Fe nucleus is located, due to the spatial redistribution of the charge of the surrounding atoms.

The appearance of a relaxation sextet in the LS20-NS sample could be due to the partial transition state of the sample – the Curie temperature. Similar features are encountered in the investigations of analogous compounds samples. According to literature, it is due to lattice distortions [42], where Fe ions are located in a defect structure or at the grain boundary (presence of Fe atoms with different numbers of Fe-Mn neighbors). Rojo et al. suppose that it can be seen as a superposition of two ferromagnetic phases with different T_C. [43] The presence of both ferromagnetic and paramagnetic or relaxed contributions was also showed in [44]. Others demonstrated two components in the manganite: ferromagnetic metal and paramagnetic insulator [45]. We suppose that in our case at x=0.20 the rhombohedral phase of perovskite consists of different size clusters with possibility of a small magnetic contribution of fine particles (relaxation sextet) where Fe^{3+} positions are with small hyperfine field, and small clusters have fast fluctuations of their magnetic moment. In previous works devoted to Ca-doped manganite oxides [41,46,47] we discovered formation of superparamagnetic clusters at 80 K inspired by [48] observations, where authors detected spontaneous formation of localized magnetic clusters using SANS measurements. Here, when the temperature is lowered from 300 K to 80 K the appearance of broad lines in Mössbauer spectra, accompanied by the transformation of paramagnetic doublet into magnetically ordered sextet with a relaxation character. Processing 80 K Mössbauer spectra was carried out by hyperfine magnetic field distribution using the model of many-state superparamagnetic relaxation [49], parameters are presented in Table 3. Within the framework of this model, the process of relaxation between different values of the projection of the spin onto the axis of the easiest magnetization is described, while the rate of jump of the projection of the spin is described by hyperfine parameter - the relaxation frequency ln(*R*).

We suppose, that the relaxation character of the spectra is due to the presence of small magnetic clusters of different sizes which behave like superparamagnetic particles. Thus, in our case, the model describes the oscillations of the magnetic moment not of one particle, but of clusters. Using many-state superparamagnetic relaxation model, it is possible to obtain the properties of the clusters calculated from relaxation parameter α which is the ratio of the magnetic-anisotropy energy to the thermal-oscillation energy: $\alpha = \frac{K_{eff}V}{k_B T}$ (K_{eff} is effective magnetic anisotropy constant, V – the cluster volume, k_{B} – the Boltzmann constant, T – the temperature). As Sr amount increases, the calculated relaxation parameter α increases too. The hyperfine magnetic field at nucleus also increases whereas the distribution of width at half height decreases. We assume that this is due to a decrease in δ and Mn^{4+} content. The value of ln(R) is approximately the same for the three samples and equals to 20.

Samples of stoichiometric composition obtained after vacuum annealing are presented in the model of the phase-separated system. The processing of 300 K Mössbauer spectra of LS5-S [41], LS5*, LS10-S samples was carried out in two ways: 1) by extracting the distribution of quadrupole splittings, and further model interpretation of the distribution; 2) model fitting by three or two quadrupole doublets. LS20-S spectra was also proceed in two steps as well: using the same model like for LS20-NS, and fitting by a combination of quadrupole doublet and a relaxation type sextet. Mössbauer spectra and their corresponding distributions p(Δ) are shown in Fig. 4,5. The p(Δ) distributions for LS5-S and LS10-S samples have a noticeable character, which indicates the formation of phase-separated state consisting of orthorhombic phases. According to our previous investigations [47], the peak in p(Δ) with the maximum value of Δ corresponds to a local environment of the *PnmaII* phase (with the maximum lattice distortions associated with the Jahn-Teller effect). In the other hand, the peak with a minimum value of Δ – could be assigned to the *PnmaI* phase with minimal distortion of the environment. Finally, the peak with intermediate value is associated with the *PnmaII** phase. Thus, for LS5-S sample the shape of the distribution is rather wide, with two visible peaks at Δ ~ 0.58 mm/s and Δ ~ 0.87 mm/s, corresponding to *PnmaII** and *PnmaII* phases respectively. In LS5* two distribution main peaks are observed with significant overlapping. They correspond to the phases *PnmaI* (Δ ~ 0.33 mm/s) and *PnmaII** (Δ ~ 0.52 mm/s). This means that after 8 hours annealing, a phase transition from the *R-3c* phase into a mixture of *PnmaI* and *PnmaII** phases occurs, *PnmaII* phase is not formed due to the excess of oxygen presence.

The distribution of the LS10-S sample most clearly demonstrates phase separation – three different peaks are clearly visible: peak at Δ ~ 0.23 mm/s for *PnmaI* phase, Δ ~ 0.50 mm/s for *PnmaII** phase and small one Δ ~ 0.95 mm/s for *PnmaII*. The LS20-S distribution is presented with one distinct peak, corresponding to *R-3c* phase (Δ ~ 0.23 mm/s). As in the case of the LS20-NS sample, in addition to p(Δ) distribution, there is a relaxation type sextet with a 62 kOe hyperfine magnetic field. It can be argued that with 20% Sr content the formation of orthorhombic phases does not occur and regardless of annealing, the LS20-S sample is structurally almost the same as LS20-NS. Such fitting allowed the identification of the phase presence based on the values of the quadrupole splitting of the peaks. To obtain quantitative information about the contributions of each phase, the fitting of the distributions presented in the form of a spectrum was carried out. In Table 4 obtained parameters are presented: the quadrupole splitting Δ, and the relative intensity of each phase *I*. The second way for spectrum processing is model fitting by the combination of three or two quadrupole doublets Fig. 4 (a,b,c), Fig. 5 (j). The parameters obtained practically coincide with those obtained by the first way. This supports the correctness of applying both models.

Measurements of annealed samples at 80 K were carried out. Fit the spectra of LS5-S sample by a magnetic field distribution in Hamilton model and one relaxation subspectrum in many-state superparamagnetic relaxation model were used, LS10-S – magnetic field distribution in Hamilton model and two relaxation sextets were used. Hamilton model is used when the energy of the quadrupole interaction is sufficiently high compare to the energy of the magnetic interaction, and, accordingly, in a situation where there is a violation of the equidistance in the arrangement of the spectrum components in the Doppler velocity scale. In our case, the reason for using Hamiltonian model was the presence of a large value of the quadrupole splitting for the *PnmaII* phase spectrum. Fitting the spectra of LS5* sample by two relaxation subspectra in many-state superparamagnetic relaxation model were used. The LS20-S spectrum was processed by extracting the distribution of the hyperfine magnetic field using the model of many state superparamagnetic relaxation.

The parameters of all subspectra are given in Table 4. As shown above, in the LS5-S, the *PnmaII** phase prevails, the *PnmaII* phase is almost suppressed. It can be assumed that in the low-temperature spectrum for this sample, the sextet with maximum intensity corresponds to the *PnmaII** phase. For LS5* the contributions of the orthorhombic phases *PnmaII** and *PnmaI* are almost the same. For the LS10-S

sample the predominant phase is *PnmaI*. Above 10% of Sr, all orthorhombic phases disappear.

By the analogy with previous work [41], we assume that at low temperature the magnetic hyperfine field decreases in the series H_n(*PnmaI*) > H_n(*PnmaII**) > H_n(*PnmaII*). As for the non-stoichiometric samples, the relaxation components are connected with the presence of magnetic clusters. Here, it can be noted that, in comparison with samples of non-stoichiometric composition, the calculated values of the relaxation frequency are lower in samples of stoichiometric composition. However, the relaxation frequency in all samples is rather small, which may indicate that the clusters are actually still in a blocked state. To confirm, in addition, LS5-S spectrum was measured at the T= 5 K, and it showed a sextet (Fig. 6, Table 4). Consequently, the blocking temperature T_b for magnetic clusters is above 5 K.

Thus, it can be argued that, after annealing, the system is distinguished by an unusual phase transition, where one rhombohedral phase passes into a mixture of three or two orthorhombic phases, that is, phase separation occurs. As the Sr concentration in the samples increases, the *PnmaII* phase transfers to the *PnmaI* phase through the intermediate orthorhombic *PnmaII** phase.

3.3. Magnetic measurements

3.3.1 Magnetic susceptibility

Figure 7 shows the temperature dependences of the AC magnetic susceptibility and its inverted values measured for all investigated samples in the range 70-275 K. Single-phase LS-NS and LS-20S samples demonstrate temperature paramagnetic to ferromagnetic phase transition in the range of 170-270K. From the intersection of the straight line approximating the linear portion of the inverse dependence $1/\chi$, Curie temperature was determined for each sample under investigation. T_C increases gradually with Sr doping content (Table 5). The slope of the linear approximation of the inverse magnetic susceptibility above *T*c also decreases with higher doping content. As the slope angle equals the inverted Curie constant, which is proportional to the magnetic moments per atom and taking into account the higher magnetic moments of Mn^{3+} (2 μB) compared to Mn^{4+} (1.5 μB), change in Mn^{3+}/Mn^{4+} ratio with doping could explain the increase in the slope of the susceptibility in paramagnetic region. It should be noted that at x=0.2 we observe approximately the same Curie temperature for both LS20-NS and LS20-S samples. It means that

regardless of the interstitial oxygen, at x =0.2, the limiting volume value is reached for obtaining stoichiometry in the sample.

Temperature dependence of magnetic susceptibility of LS5-S, LS5* and LS10-S samples has peaks due to AFM – PM transition. For pure antiferromagnetic phase as in the case of LS5-S the peak is narrow. LS5* sample demonstrates broad peak of the magnetic susceptibility which can be attributed to the AFM-PM transition of the *PnmaII** phase and FM-PM transition of the *PnmaI* phase. The peak widening can be caused by local lattice distortions. The inverse susceptibility dependence for this sample also has the linearly increasing portion, indicating the presence of the ferromagnetic phase (*PnmaI*) with T_C =150 K. The contribution of ferromagnetic phase disappears with further annealing of the sample with 5% of Sr doping. The peculiarity of the inverse susceptibility dependence above Neel temperature (the upward curvature) described in [50] was caused by the contribution of superparamagnetic clusters to the magnetic response of the sample, that supports the considered model of magnetic structure of the samples. The sample LS10-S behaves similar to the LS5* sample, demonstrating the contributions of AFM and FM phases, however, two characteristic peaks for the Neel temperature are observed in the LS10-S sample. Neel temperature for the stoichiometric samples is approximately the same, and not dependent of Sr content. The values obtained are also similar to the temperatures obtained for the pure $LaMnO_3$ [51,52].

3.3.2 Magnetostatic properties and magnetization temperature sweep

For the understanding of the effect of doping and annealing on the response of Sr doped manganites, magnetostatic properties were investigated (Fig. 8). For the non-stoichiometric samples hysteresis loops measured at 100K have shape typical for ferromagnets. Saturation magnetization slightly increases with increasing Sr content. Such dependence can be caused by the slight decrease of Mn^{4+} amount in the samples with doping. The same reason explained the behavior of the *T*c and the slope of the paramagnetic region of inverse susceptibility with doping. With temperature increase the transformation of magnetic response was observed. At 300K LS5-NS sample demonstrates paramagnetic behavior. On the magnetization curve for the sample LS10-NS there is a weak kink inherent to low ferromagnetic contribution. For the sample LS20-NS hysteresis was observed even at room temperature. These results are consistent with the results of Mössbauer investigations. For the sample with 20% Sr content the

spectra contained the relaxation type sextet. The relative contribution of the residual ferromagnetic component in the sample with 10% Sr was much lower and was not distinguished in the Mössbauer spectra. As the values of Curie temperatures obtained from the inverse susceptibility dependences for these samples are close to room temperature, the residual magnetic ordering can be observed. It should also be noted, that in the doped manganite samples the appearance of superparamagnetic clusters above room temperature was previously reported [41]. Magnetization curves for all samples measured at 400K demonstrate paramagnetic behavior. Annealed LS20-S sample shows the same features as the non-stoichiometric sample with the same Sr content. It was discussed above, that the results of X-ray diffraction, Mössbauer investigations and susceptibility measurements also show similarity of these two samples.

Hysteresis loop for the LS5* sample measured at 100K is characterized by large contribution of the ferromagnetic phase and larger value of coercivity (100 Oe) than LS5-NS (20 Oe), which can be attributed to stronger anisotropy of the powder. The additional anisotropy can be explained by the exchange interaction between ferromagnetic and antiferromagnetic phases. At higher temperatures the sample demonstrates linear magnetization dependence. As was described in the previous section, Neel and Curie temperatures for AFM and FM phases of this samples are 120 K and 150 K, respectively. LS10-S sample shows similar response, which can be explained by the similar phase composition of the sample. The coercivity for the sample with 10% of Sr increases from 25 Oe to 170 Oe.

Hysteresis loop of the LS5-S sample has the shape typical for samples with antiferromagnetic type of ordering with uncompensated magnetic moment. The coercivity of the sample is an order of magnitude larger – it exceeds 500 Oe. Saturation is not achieved in the investigated magnetic field range. The origin of uncompensated magnetic moment could lie in the formation of low-dimensional clusters with ferromagnetic ordering due to local lattice distortions.

Temperature dependences of magnetization measured in ZFC-FC regime (Fig. 9) were used to determine the temperature, at which the energy of thermal fluctuations is comparable with the anisotropy energy (blocking temperature T_b). According to the type of temperature dependences behavior, there is a discrepancy between ZFC and FC, which indicates the presence of an uncompensated magnetic moment,

caused in general case by CAF and due to the presence of superparamagnetic phenomena [17,20,22–24,34,53]. We suppose, that the formation of magnetic clusters or/and spin-canting at the surface of the particles can be responsible for such behavior in our samples. Exchange interaction frustrations of the cluster with the matrix can lead to relaxation behavior of the magnetic moment of the cluster.

The effective anisotropy constant can be estimated using the shape of the magnetization curve. According to Akulov's law [54], the saturation approximation region of $M(H)$ dependence in the system of randomly oriented crystallites can be expressed as follows: $\frac{M(H)}{M_S} = 1 - \left(\frac{2aK_{eff}}{M_S H}\right)^2$. Here M_S is saturation magnetization, a is symmetry parameter, describing the special distribution of easy magnetization axes, K_{eff} is the effective anisotropy constant, H is magnetic field. To take the paramagnetic contribution into account additional linear term with B slope can be included. Thus, fitting the magnetization curve in the range of saturation approximation with the function $M(H) = A + B * H - \frac{C}{A} * \frac{1}{H^2}$ with the use A = M_S, B and C as fitting parameters, allows us to obtain the value of K_{eff} from the C parameter. To increase fitting accuracy, A and B were determined from the linear approximation $M(H) = A + B * H$ of the saturated region of magnetization curve and then were used as fixed parameters. The symmetry parameter a was taken equal to $a = \frac{1}{\sqrt{15}}$, which corresponded to systems of particles with uniaxial anisotropy with a random distribution of the easy magnetization axes. Thus, C corresponded to K_{eff}^2, and the effective anisotropy constant was calculated as a square root of fitting parameter C.

Using the anisotropy constant, which were determined from the magnetization curves by Akulov's law approximation, one can determine the effective volume blocked under the T_b. In all the cases linear dimensions of the blocked region corresponded to the smaller volume, than the size of the particle, describing the regions of uncompensated magnetic moment (the contribution of ferromagnetic clusters and spin-canted regions). Results of calculation and analysis of the magnetic cluster size from Mössbauer and magnetic data shown in Table 5. The clusters size for rhombohedral phases don't depend on Sr content, equals 5.7 nm. Cluster sizes for stoichiometric samples are less in orthorhombic phases in LS10-S and LS5*and vary from 3.9 to 4.9 nm.

Figure 10 shows the magnetic phase diagram for $La_{1-x}Sr_xMnO_3$ (x =0.05, 0.10, 0.20), including the magnetic ordering temperatures of the studied system, as well as data obtained from literary sources [19,55–62]. It can be seen that the Neel temperatures T_N practically do not change with increasing concentration of Sr, which characterizes a fairly wide range of magnetic transitions. The Curie temperatures T_C increase with increasing x (large value of dT_C/dx determined). An increase in the concentration of the alloying element leads to an increase in the ferromagnetic order in the system.

4. Conclusion

New structural and magnetic properties of perovskite oxides $La_{1-x}Sr_xMnO_{3+\delta}$ (x = 0.05, 0.10, 0.20) are detected via the complementary data from Mossbauer spectroscopy, magnetization, magnetic susceptibility measurements and SEM techniques.

The synthesized samples via sol-gel method are single-phase (*R-3c*). After annealing for 10-15 hours, all samples become stoichiometric ($\delta = 0$), except the sample with x = 0.20 which retains its structure, they transform into a phase-separated system as a mixture of orthorhombic phases: (*PnmaII**, *PnmaII*) for x = 0.05 and (*PnmaI*, *PnmaII**, *PnmaII*) for x = 0.10. Wherein the sample with x = 0.05 annealed in vacuum for 8 hours also becomes two-phase but with a different set of phases (*PnmaI*, *PnmaII**) with properties close to those of the annealed sample with x = 0.10. This is due to the insufficient duration of annealing and as a consequence the presence of the excess oxygen in the sample ($\delta > 0$), which leads to an increase in the concentration of Mn^{4+} ions. Taking into account the influence of annealing time can be useful in planning technological processes for creating materials with the required properties.

The difference between studied structural modifications consists in different degrees of lattice distortion, Mn-O lengths of bonds, as well as the existence of different magnetic ordering. It can be concluded that for annealed samples, with increasing Sr content, the orbital order associated with the Jahn-Teller effect is rapidly destroyed. At x > 0.10, only the orthorhombic *PnmaI* phase is formed with a higher symmetry of the environment while only the rhombohedral phase is formed for x = 0.20.

With a small Sr doping for La, the Mn^{3+}–O^{2-}–Mn^{3+}superexchange interactions dominate, which lead to an anisotropic antiferromagnetic interaction. As x increases, the Mn^{3+}–O^{2-}–Mn^{4+} double exchange interaction in the magnetic sublattice increase due to an increase in the Mn^{4+} content. Ferromagnetic ordering appears in samples with $x > 0.1$.

Anisotropy of ferromagnetic contribution caused by exchange anisotropy of interacting ferromagnetic and antiferromagnetic phases in the samples was revealed. At temperatures below magnetic ordering, all perovskite phases contain nanosized magnetic clusters. Frustration of the exchange interaction of the cluster with the matrix can lead to relaxation behavior of the magnetic moment of the cluster.

The clusters size in *R-3c* phase is the same equals to 5.7 nm; their size is less in orthorhombic phases and vary from about 3.9 to 4.9 nm. All samples are characterized by the presence of particles agglomerates with a typical size about 0.4-0.8 μm; for annealed samples additional non-conducting regions with 80-220 nm in size were found.

Declaration of interests

The authors declare that they have no known competing financial interests or personal relationships that could have appeared to influence the work reported in this paper.

Acknowledgments

Diana Pchelina is a scholarship holder of the Foundation for the Development of Theoretical Physics and Mathematics "BASIS" №21-2-2-37-1.

References

[1] J.M.D. Coey, M. Viret, S. Von Molnár, Mixed-valence manganites, Adv. Phys. 48 (1999) 167–293. https://doi.org/10.1080/000187399243455.

[2] A. Moreo, S. Yunoki, E. Dagotto, Phase Separation Scenario for Manganese Oxides and Related Materials, Science (80-.). 283 (1999) 2034–2040. https://doi.org/10.1126/SCIENCE.283.5410.2034.

[3] E.L. Nagaev, Colossal-magnetoresistance materials: manganites and conventional ferromagnetic semiconductors, Phys. Rep. 346 (2001) 387–531. https://doi.org/10.1016/S0370-1573(00)00111-3.

[4] S.S.P. Parkin, Giant Magnetoresistance in Magnetic Nanostructures, Annu. Rev. Mater. Sci. 25 (1995) 357–388. https://doi.org/10.1146/annurev.ms.25.080195.002041.

[5] R.J. Singh, Some Important Features of Manganites, J. Mod. Phys. 04 (2013) 191–199. https://doi.org/10.4236/jmp.2013.42027.

[6] N. Rezlescu, E. Rezlescu, C. Doroftei, P.D. Popa, M. Ignat, NANOSTRUCTURED LANTHANUM MANGANITE PEROVSKITES IN CATALYST APPLICATIONS, J. Nanomater. Biostructures. 8 (n.d.) 581–587.

[7] K. Huang, J. Wan, J.B. Goodenough, Oxide-ion conducting ceramics for solid oxide fuel cells, J. Mater. Sci. 2001 365. 36 (2001) 1093–1098. https://doi.org/10.1023/A:1004813305237.

[8] H. Szymczak, R. Szymczak, Magnetocaloric effect. Physics and applications, Mater. Sci. 26 (2008).

[9] B. Sahoo, D. Behera, Investigation of superconducting and elastic parameters of YBCO/LSMO thick films, J. Mater. Sci. Mater. Electron. 2019 3014. 30 (2019) 12992–13004. https://doi.org/10.1007/S10854-019-01661-X.

[10] D. Juan, M. Pruneda, V. Ferrari, Localized electronic vacancy level and its effect on the properties of doped manganites, Sci. Reports 2021 111. 11 (2021) 1–11. https://doi.org/10.1038/s41598-021-85945-5.

[11] M.M. Mikhailov, V.A. Vlasov, T.A. Utebekov, A.N. Sokolovskiy, A.A. Lovizkii, A.E. Smolin, Solid-state synthesis of LaSrMnO3 powders for smart coatings, Mater. Res. Bull. 89 (2017) 154–160. https://doi.org/10.1016/j.materresbull.2017.01.038.

[12] A.S. Davydov, A. V. Belousov, G.A. Krusanov, M.A. Kolyvanova, B.B. Kovalev, A.S. Komlev, P. V. Krivoshapkin, V.N. Morozov, V.I. Zverev, Promising magnetic nanoradiosensitizers for combination of tumor hyperthermia and x-ray therapy: Theoretical calculation, J. Appl. Phys. 129 (2021) 033902. https://doi.org/10.1063/5.0032843.

[13] M.C. Ferreira, B. Pimentel, V. Andrade, V. Zverev, R.R. Gimaev, A.S. Pomorov, A. Pyatakov, Y. Alekhina, A. Komlev, L. Makarova, N. Perov, M.S. Reis, Understanding the Dependence of Nanoparticles Magnetothermal Properties on Their Size for Hyperthermia Applications: A Case Study for La-Sr Manganites, Nanomater. 2021, Vol. 11, Page 1826. 11 (2021) 1826. https://doi.org/10.3390/NANO11071826.

[14] J. Kanamori, Superexchange interaction and symmetry properties of electron orbitals, J. Phys. Chem. Solids. 10 (1959) 87–98. https://doi.org/10.1016/0022-3697(59)90061-7.

[15] E.L. Nagaev, Lanthanum manganites and other giant-magnetoresistance magnetic conductors, Physics-Uspekhi. 39 (1996) 781. https://doi.org/10.1070/PU1996V039N08ABEH000161.

[16] G.H. Jonker, J.H. Van Santen, Ferromagnetic compounds of manganese with perovskite structure, Physica. 16 (1950) 337–349. https://doi.org/10.1016/0031-8914(50)90033-4.

[17] M. Pissas, G. Papavassiliou, The phase diagram and magnetic properties of La1-xCa xMnO3 compounds for $0 \leq x \leq 0.23$, J. Phys. Condens. Matter. 16 (2004) 6527–6540. https://doi.org/10.1088/0953-8984/16/36/018.

[18] J.D. Lee, B.I. Min, Charge ordering in doped manganese oxides: lattice dynamics and magnetic structure, (1997).

[19] Q. Huang, A. Santoro, J. Lynn, Structure and magnetic order in undoped lanthanum manganite, Phys. Rev. B - Condens. Matter Mater. Phys. 55 (1997) 14987–14999. https://doi.org/10.1103/PhysRevB.55.14987.

[20] J. Töpfer, J.B. Goodenough, LaMnO3+δRevisited, J. Solid State Chem. 130 (1997) 117–128. https://doi.org/10.1006/JSSC.1997.7287.

[21] D. Pchelina, V. Sedykh, O. Rybchenko, B. Fraisse, M.T. Sougrati, In situ high temperature XRD study of Sr-doped ceramics La0.95Sr0.05MnO3+δ, Solid State Commun. 336 (2021) 114401. https://doi.org/10.1016/J.SSC.2021.114401.

[22] H. Kawano, R. Kajimoto, M. Kubota, H. Yoshizawa, Ferromagnetism-induced reentrant

structural transition and phase diagram of the lightly doped insulator), Phys. Rev. B - Condens. Matter Mater. Phys. 53 (1996) R14709–R14712. https://doi.org/10.1103/PHYSREVB.53.R14709.

[23] Y. Yamada, O. Hino, S. Nohdo, R. Kanao, T. Inami, S. Katano, Polaron Ordering in Low-Doping La1-xSrxMnO3, Phys. Rev. Lett. 77 (1996) 904–907. https://doi.org/10.1103/PHYSREVLETT.77.904.

[24] S. Reschke, F. Mayr, S. Widmann, M. Paraskevopoulos, F. Mayr, J. Hemberger, A. Loidl, R. Heichele, D. Maurer, V. Müller, A.A. Mukhin, A.M. Balbashov, Magnetic properties and the phase diagram of La1-xSrxMnO3 for x⩽ 0.2, Iopscience.Iop.Org. 12 (2000) 3993–4011.

[25] V. Sedykh, G.E. Abrosimova, V.S. Shekhtman, I.I. Zver'Kova, A. V. Dubovitskii, V.I. Kulakov, Phase transition from Pnma I to Pnma II in the 57Fe-doped LaMnO3+δ compound, Phys. C Supercond. Its Appl. 418 (2005) 144–150. https://doi.org/10.1016/j.physc.2004.11.020.

[26] M.M. Schmitt, Y. Zhang, A. Mercy, P. Ghosez, Electron-lattice interplays in LaMnO 3 from canonical Jahn-Teller distortion notations, (n.d.).

[27] V.D. Sedykh, The features of structural transformations in lanthanum manganites La1-xAxMnO3+δ (A = Ca, Sr, Ba), in: AIP Conf. Proc., American Institute of Physics Inc., 2014: pp. 72–80. https://doi.org/10.1063/1.4898613.

[28] V.D. Sedykh, I.I. Zver'kova, V.S. Shekhtman, A. V. Dubovitskiĭ, V.I. Kulakov, Mössbauer and X-ray studies of the structural phase transformations and suppression of polymorphism in La1 − x Sr x Mn0.98Fe0.02O3 + δ (x = 0.05–0.30), Phys. Solid State. 52 (2010) 591–598. https://doi.org/10.1134/S1063783410030212.

[29] V.D. Sedykh, I.Y. Medvetskaya, D.I. Pchelina, N.I. Chistyakova, V.S. Rusakov, Y.A. Alekhina, Mössbauer and Magnetic Study of Lanthanum Manganite La1 –xCaxMn0.98Fe0.02O3 + δ (x = 0.05, 0.10, 0.20): Nonstoichiometric and Stoichiometric Composition, Crystallogr. Reports. 65 (2020) 347–351. https://doi.org/10.1134/S1063774520030293.

[30] V. Sedykh, V.S. Shekhtman, I.I. Zverkova, A. V. Dubovitskii, V.I. Kulakov, Reversibility of structure phase transitions in LaMnO3+δ manganite under heat treatment, Phys. C Supercond. Its Appl. 433 (2006) 189–194. https://doi.org/10.1016/j.physc.2005.10.013.

[31] V.D. Sedykh, V.S. Shekhtman, A. V. Dubovitskiĭ, I.I. Zver'Kova, V.I. Kulakov, Mössbauer and

X-Ray studies of the dynamics of phase transformations and suppression of polymorphism in the LaMn1 - X Fe x O3 + δ compound (x = 0.015-0.500), Phys. Solid State. 51 (2009) 373–380. https://doi.org/10.1134/S1063783409020280.

[32] M.E. Matsnev, V.S. Rusakov, SpectrRelax: An application for Mössbauer spectra modeling and fitting, in: AIP Conf. Proc., American Institute of PhysicsAIP, 2012: pp. 178–185. https://doi.org/10.1063/1.4759488.

[33] D. Drobac, On the determination of the Curie temperature from AC susceptibility measurement, J. Magn. Magn. Mater. 183 (1998) 71–74. https://doi.org/10.1016/S0304-8853(97)01100-1.

[34] A. Urushibara, Y. Moritomo, T. Arima, A. Asamitsu, G. Kido, Y. Tokura, Insulator-metal transition and giant magnetoresistance in La1-xSrxMnO3, Phys. Rev. B. 51 (1995) 14103–14109. https://doi.org/10.1103/PHYSREVB.51.14103.

[35] K. Kumagai, A. Iwai, Y. Tomioka, H. Kuwahara, Y. Tokura, A. Yakubovskii, Microscopically homogeneous magnetic structure of (formula presented) beyond the range of (formula presented) observed by la nmr, Phys. Rev. B - Condens. Matter Mater. Phys. 59 (1999) 97–99. https://doi.org/10.1103/PHYSREVB.59.97.

[36] S. V Trukhanov, I.O. Troyanchuk, A. V Trukhanov, H. Szymczak, R. Szymczak, M. Baran, Magnetic and electrotransport properties of the anion-deficient manganites with perovskite structure, Springer. 139 (2005) 461–478. https://doi.org/10.1007/s10909-005-4734-1.

[37] J.A. Souza, J.J. Neumeier, R.K. Bollinger, B. McGuire, C.A.M. Dos Santos, H. Terashita, Magnetic susceptibility and electrical resistivity of LaMn O3, CaMn O3, and La1-x Srx Mn O3 (0.13 x 0.45) in the temperature range 300-900 K, Phys. Rev. B - Condens. Matter Mater. Phys. 76 (2007). https://doi.org/10.1103/PHYSREVB.76.024407.

[38] V.D. Sedykh, V.S. Rusakov, I.I. Zver'kova, A. V. Dubovitskii, V.I. Kulakov, Specific features of the structural transformations in La1-xCaxMn0.9857Fe0.02O3+δ (x = 0.05-0.50), Phys. Solid State. 53 (2011) 1440–1447. https://doi.org/10.1134/S1063783411070237.

[39] J. Töpfer, J.B. Goodenough, LaMnO3+δ Revisited, J. Solid State Chem. 130 (1997) 117–128. https://doi.org/10.1006/jssc.1997.7287.

[40] V.K. Karpasyuk, A.G. Badelin, D.I. Merkulov, I.M. Derzhavin, S.K. Estemirova, Unusual properties and features of oxygen nonstoichiometry of La-Sr manganites with manganese

replacement by a combination of nickel and germanium, J. Phys. Conf. Ser. 1347 (2019) 012036. https://doi.org/10.1088/1742-6596/1347/1/012036.

[41] D. Pchelina, V. Sedykh, N. Chistyakova, V. Rusakov, Y. Alekhina, A. Tselebrovskiy, B. Fraisse, L. Stievano, M.T. Sougrati, Alkaline-earth metal-doped perovskites La0.95A0.05MnO3+δ (A = Ca, Sr): New structural and magnetic features revealed by 57Fe Mössbauer spectroscopy and magnetic measurements, J. Phys. Chem. Solids. 159 (2021) 110268. https://doi.org/10.1016/J.JPCS.2021.110268.

[42] B. Hannoyer, G. Marest, J.M. Greneche, R. Bathe, S.I. Patil, S.B. Ogale, Colossal magnetoresistance and hyperfine interactions in iron-doped <span class, Phys. Rev. B. 61 (2000) 9613. https://doi.org/10.1103/PhysRevB.61.9613.

[43] J.M. Barandiarán, J.M. Greneche, T. Hernández, F. Plazaola, T. Rojo, Non-conventional magnetic order in Fe-substituted La0.7Sr0.3MnO3giant-magnetoresistance manganites, J. Phys. Condens. Matter. 14 (2002) 12563. https://doi.org/10.1088/0953-8984/14/47/328.

[44] M. Pissas, G. Kallias, E. Devlin, A. Simopoulos, D. Niarchos, Mössbauer study of La0.75Ca0.25Mn0.98Fe0.02O3 compound, J. Appl. Phys. 81 (1997) 5770. https://doi.org/10.1063/1.364722.

[45] M. Uehara, S. Mori, C.H. Chen, S.-W. Cheong, Percolative phase separation underlies colossal magnetoresistance in mixed-valent manganites, Nat. 1999 3996736. 399 (1999) 560–563. https://doi.org/10.1038/21142.

[46] D.I. Pchelina, I.Y. Medvetskaya, N.I. Chistyakova, V.S. Rusakov, V.D. Sedykh, Y.A. Alekhina, Mössbauer and Magnetic Studies of Doped Lanthanum Manganite La1 – xCaxMn0.98Fe0.02O3 + δ (x = 0.05, 0.10, 0.20): I. Nonstoichiometric Composition, J. Surf. Investig. 12 (2018) 1047–1051. https://doi.org/10.1134/S1027451018050476.

[47] D.I. Pchelina, I.Y. Medvetskaya, N.I. Chistyakova, V.S. Rusakov, V.D. Sedykh, Y.A. Alekhina, Mössbauer and Magnetic Studies of Doped Lanthanum Manganite La1 – xCaxMn0.98Fe0.02O3 (x = 0.05, 0.10, 0.20): II. Stoichiometric Composition and Phase Segregation, J. Surf. Investig. 13 (2019) 462–468. https://doi.org/10.1134/S1027451019030303.

[48] J.M. De Teresa, M.R. Ibarra, P.A. Algarabel, C. Ritter, C. Marquina, J. Blasco, J. Garcia, A. del Moral, Z. Arnold, Evidence for magnetic polarons in the magnetoresistive perovskites, Nature.

386 (1997) 256–259.

[49] D.H. Jones, K.K.P. Srivastava, Many-state relaxation model for the Mössbauer spectra of superparamagnets, Phys. Rev. B. 34 (1986) 7542–7548. https://doi.org/10.1103/PhysRevB.34.7542.

[50] M. Muroi, R. Street, Evolution of Ferromagnetism in LaMnO3+δ, Aust. J. Phys. 52 (1999) 205–225. https://doi.org/10.1071/P98059.

[51] A. El-Moez A. Mohamed, P. Álvarez-Alonso, B. Hernando, The intrinsic exchange bias effect in the LaMnO3 and LaFeO3 compounds, J. Alloys Compd. 850 (2021) 156713. https://doi.org/10.1016/J.JALLCOM.2020.156713.

[52] V. Markovich, E. Rozenberg, G. Gorodetsky, G. Jung, I. Fita, R. Puzniak, A. Wisniewski, C. Martin, S. Hebert, B. Raveau, Vacancies at Mn-sites in LaMn1−xO3 manganites: Interplay between ferromagnetic interactions and hydrostatic pressure, J. Appl. Phys. 95 (2004) 7112. https://doi.org/10.1063/1.1667855.

[53] J. Mitchell, D. Argyriou, C. Potter, D. Hinks, J. Jorgensen, S. Bader, Structural phase diagram of: Relationship to magnetic and transport properties, Phys. Rev. B - Condens. Matter Mater. Phys. 54 (1996) 6172–6183. https://doi.org/10.1103/PHYSREVB.54.6172.

[54] N.S. Akulov, Über den Verlauf der Magnetisierungskurve in starken Feldern, Zeitschrift Für Phys. 69 (1931) 822–831. https://doi.org/10.1007/BF01339465.

[55] M. Paraskevopoulos, F. Mayr, J. Hemberger, A. Loidl, R. Heichele, D. Maurer, V. Muller, A. Mukhin, A.M. Balbashov, Magnetic properties and the phase diagram of La1−xSrxMnO3 for x 0.2, J. Phys. Condens. Matter. 12 (2000) 3993–4011.

[56] K. De, S. Das, A. Roy, P. Dhak, M. Willinger, J.S. Amaral, S. Giri, S. Majumdar, C.J.R. Silva, M.J.M. Gomes, P.K. Mahapatra, Enhanced ferromagnetism and glassy state in phase separated La0.95Sr0.05MnO3+d, J. Appl. Phys. 112 (2012) 1–6.

[57] N.I. Solin, L.N. Romashev, S. V. Naumov, A.A. Saranin, A. V. Zotov, D.A. Olyanich, V.G. Kotlyar, O.A. Utas, Magnetoresistive properties of nanostructured magnetic metals, manganites, and magnetic semiconductors, Tech. Phys. 61 (2016) 233–239. https://doi.org/10.1134/S1063784216020237.

[58] J. Blasco, J. García, J. de Teresa, M. Ibarra, J. Perez, P. Algarabel, C. Marquina, C. Ritter,

Structural, magnetic, and transport properties of the giant magnetoresistive perovsk, Phys. Rev. B - Condens. Matter Mater. Phys. 55 (1997) 8905–8910. https://doi.org/10.1103/PhysRevB.55.8905.

[59] A. Urushibara, Y. Moritomo, T. Arima, A. Asamitsu, G. Kido, Y. Tokura, Insulator-metal transition and giant magnetoresistance in La1-xSrxMnO3, Phys. Rev. B. 51 (1995) 14103–14109. https://doi.org/10.1103/PhysRevB.51.14103.

[60] L.I. Koroleva, D.M. Zashchirinskiĭ, T.M. Khapaeva, L.I. Gurskiĭ, N.A. Kalanda, V.M. Trukhan, R. Szymczak, B. Krzumanska, Effect of oxygen deficiency on the magnetic, electrical, magnetoelectric, and magnetoelastic properties of La1 - X Sr x MnO 3 - δ manganites, Phys. Solid State. 50 (2008) 2298–2302. https://doi.org/10.1134/S1063783408120123.

[61] S. Das, J.S. Amaral, K. De, M. Willinger, J.N. Gonçalves, A. Roy, P. Dhak, S. Giri, S. Majumder, C.J.R. Silva, M.J.M. Gomes, P.K. Mahapatra, V.S. Amaral, Strain induced enhanced ferromagnetic behavior in inhomogeneous low doped La0.95Sr0.05MnO3+δ, Appl. Phys. Lett. 102 (2013) 0–4. https://doi.org/10.1063/1.4793657.

[62] K. McBride, J. Cook, S. Gray, S. Felton, L. Stella, D. Poulidi, Evaluation of La1-xSrxMnO3 ($0 \leq x < 0.4$) synthesised via a modified sol-gel method as mediators for magnetic fluid hyperthermia, CrystEngComm. 18 (2016) 407–416. https://doi.org/10.1039/c5ce01890k.

Figure Captions

Fig. 1. Dependence of the Mn^{4+} ions concentration on the Sr content in the compound $\mathbf{La_{1-x}^{3+}Sr_x^{2+}Mn_y^{4+}Mn_{1-y}^{3+}O_{3+\delta}^{2-}}$.

Fig. 2. SEM pictures for all samples and histograms with agglomerate size distribution with Gauss fitting.

Fig. 3.^{57}Fe Mössbauer spectra of LSM-NS measured at room temperature and 80 K (with distributions) (a,d,g – LS5-NS, b,e,h – LS10-NS and c,f,i – LS20-NS respectively).

Fig. 4. ^{57}Fe Mössbauer spectra and distributions of LSM-S measured at room temperature and 80 K (a,d,g – LS5-S, b,e,h – LS10-S and c,f,i – LS20-S respectively).

Fig. 5. ^{57}Fe Mössbauer spectra and distribution of LS5* measured at room temperature (j,k) and 80 K (l).

Fig. 6. ^{57}Fe Mössbauer spectra of LS5-S measured at 5 K.

Fig.7. Temperature dependences of the direct and inverse susceptibility for the samples a) LS5-NS, b) LS10-NS, c) LS20-NS, d) LS5-S and LS5*(blue), e) LS10-S, f) LS20-S.

Fig.8. Hysteresis loops obtained at 400, RT, 100 K for all samples.

Fig. 9. The temperature dependence of the magnetization (ZFC/FC measurements) for all samples.

Fig. 10. Magnetic phase diagram for $La_{1-x}Sr_xMnO_3$ (x = 0.05, 0.10, 0.20).

Tables

Table 1. The lattice parameters for the *R-3c*, *PnmaI*, *PnmaII** phases of $La_{1-x}Sr_xMn_{0.98}O_{3+\delta}$ (x = 0.05, 0.1, 0.2) of non-stoichiometric and stoichiometric compositions [28].

Sample	Phase	*a*, Å	*b*, Å	*c*, Å	V, Å^3	Perovskite cell volume, Å^3
$LaMnO_{3+\delta}$	*R-3c*	5.523(2)	-	13.326(4)	352.1(3)	58.68(5)
$LaMnO_3$	*PnmaII*	5.709(2)	7.714(3)	5.531(4)	243.7(3)	60.92(5)
LS5-NS	*R-3c*	5.522(2)	-	13.343(4)	352.4(3)	58.73(5)
LS10-NS	*R-3c*	5.522(2)	-	13.347(4)	352.5(3)	58.75(5)
LS20-NS	*R-3c*	5.522(2)	-	13.360(4)	352.5(3)	58.75(5)
LS5-S	*PnmaII**	5.641(2)	7.723(3)	5.539(2)	241.3(3)	60.32(8)
LS5*	*PnmaI*	5.572(2)	7.763(3)	5.541(2)	239.7(3)	59.92(8)
LS10-S	*PnmaI*	5.576(2)	7.756(3)	5.541(2)	240.0(3)	60.00(8)
LS20-S	*R-3c*	5.522(2)	-	13.360(4)	352.5(3)	58.75(5)

Table 2. Mean value and standard deviation of investigated samples, calculated from SEM pictures.

Sample	LS5-NS	LS10-NS	LS20-NS	LS5-S	LS10-S	LS20-S
$\langle d \rangle$, μm	0.837±0.015	0.580±0.010	0.440±0.009	0.885±0.014	0.628±0.011	0.442±0.010
SD, μm	0.293	0.205	0.163	0.333	0.213	0.189

Table 3. Hyperfine parameters of the ^{57}Fe 300 K and 80 K Mössbauer spectra of non-stoichiometric samples. δ – is the isomer shift relative to α-Fe at room temperature, Δ – is the quadrupole splitting, FWHM – distribution full width at middle height, H_n – is the hyperfine magnetic field, α – is the parameter of the relaxation model.

Sample	*T* = 300 K		
	δ_{max}, mm/s	Δ_{max}, mm/s	FWHM, mm/s
LS5-NS	0.366±0.002	0.276±0.024	0.340±0.011
LS10-NS	0.364±0.002	0.256±0.018	0.302±0.011
LS20-NS	0.365±0.001	0.230±0.010	0.256±0.011

Sample	T = 80 K			
	δ, mm/s	$H_{n\ max}$, kOe	FWHM, kOe	α_{max}
LS5-NS	0.499±0.006	480±3	69.6±4.5	8.8±0.7
LS10-NS	0.491±0.004	501±3	52.5±4.5	9.7±0.7
LS20-NS	0.518±0.002	517±2	45.2±4.5	10.1±0.6

Table 4. Parameters of the ^{57}Fe 300 K, 80 K and 5 K Mössbauer spectra of stoichiometric samples. δ – is the shift relative to α-Fe, Δ– is the quadrupole splitting, I – is the relative intensity of the subspectrum (contribution of each phase), H_n – is the hyperfine magnetic field, α – is the parameter of the relaxation model. The maximum spectral parameters are given in Hamilton model and for LS20-S.

Sample	T = 300 K						
Fitting		*p(Δ)*	*Distribution*		*Model fitting*		
		δ_{max}, mm/s	Δ, mm/s	*I,%*	δ, mm/s	Δ, mm/s	*I,%*
LS5-S	*PnmaII**	0.376±0.002	0.580±0.002	62.7±0.9	0.378±0.001	0.542±0.002	54.3±1.1
	PnmaII		0.875±0.002	37.3±0.9	0.377±0.001	0.857±0.002	45.7±1.1
LS5*	*PnmaI*	0.375±0.001	0.328±0.004	54.3±2.9	0.375±0.001	0.306±0.002	56.1±1.2
	*PnmaII**		0.518±0.007	45.7±2.9	0.377±0.001	0.554±0.003	43.9±1.2
LS10-S	*PnmaI*	0.373±0.001	0.226±0.001	58.5±1.4	0.373±0.001	0.225±0.002	60.9±1.5
	*PnmaII**		0.508±0.006	39.7±1.3	0.373±0.001	0.498±0.007	32.0±1.1
	PnmaII		0.948±0.015	1.9±0.7	0.373±0.001	0.812±0.015	7.1±1.0
LS20-S	*R-3c*	0.367±0.001	0.228±0.001	67.6±2.0	0.367±0.001	0.228±0.001	74.7±0.6
	R-3c relax	0.367±0.001	0.008±0.008	32.4±2.0 (H_n = 62±1 kOe)	0.367±0.001	0.008±0.009	25.3±0.6 (H_n = 63±1 kOe)

		T = 80 K			
		δ, mm/s	H_n, kOe	*α*	*I,%*
LS5-S	*PnmaII**	0.557±0.026	424±3	2.7±0.6	57.1±4.0
	PnmaII	0.484±0.004	362±3	-	42.9±4.0
LS5*	*PnmaI*	0.502±0.007	483±1	7.4±0.6	54.4±2.4
	*PnmaII**	0.476±0.015	454±2	3.8±0.4	45.6±2.4

LS10-S	*PnmaI*	0.503±0.009	492±1	3.4±0.5	55.5±2.4
	*PnmaII**	0.493±0.013	455±2	3.5±0.3	35.9±2.6
	PnmaII	0.484±0.090	379±6	-	8.6±1.6
LS20-S	*R-3c*	0.498±0.002	523±3	9.3±0.5	100

T = 5 K				
LS5-S	*PnmaII**	0.528±0.017	484±2	60.0±6.0
	PnmaII	0.489±0.026	458±3	40.0±6.0

Table 5. Curie temperatures T_C and Néel temperatures T_N, magnetic coercivity H_C, magnetic saturation M_S, K_{eff} magnetic anisotropy constant, l – approximate clusters size. For LS5-S sample the saturation is not achieved, H_C is given for particularistic loop.

Sample	T_C, K	T_N, K	H_C, Oe	M_S, emu/g	K_{eff} , J/m^3	l, nm
LS5-NS	186±2	-	18±2	68±2	$6.6*10^4$±$2.9*10^2$	5.7 (*R-3c*)
LS10-NS	226±2	-	23±2	74±2	$7.0*10^4$±$3.8*10^2$	5.7 (*R-3c*)
LS20-NS	274±2	-	38±2	78±2	$7.4*10^4$±$2.3*10^2$	5.7 (*R-3c*)
LS5-S	-	range from 122 to 125	553±2	-	-	-
LS5*	150±1	121±1	103±2	50±2	$8.7*10^4$±$4.7*10^2$	4.9 *(PnmaI)* 3.9 (*PnmaII**)
LS10-S	157±2	124±1 134±1	170±2	43±2	$7.6*10^4$±$2.3*10^2$	3.9 *(PnmaI)* 3.9*(PnmaII**)*
LS20-S	273±2	-	40±2	77±2	$7.6*10^4$±$2.3*10^2$	5.5 (*R-3c*)

Figures

Fig.1.

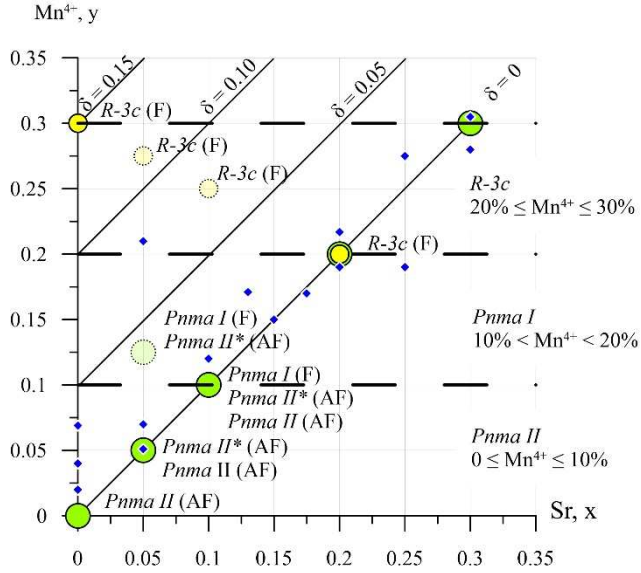

Fig. 1. Dependence of the Mn^{4+} ions concentration on the Sr content in the compound $\mathbf{La^{3+}_{1-x}Sr^{2+}_{x}Mn^{4+}_{y}Mn^{3+}_{1-y}O^{2-}_{3+\delta}}$.

Fig.2.

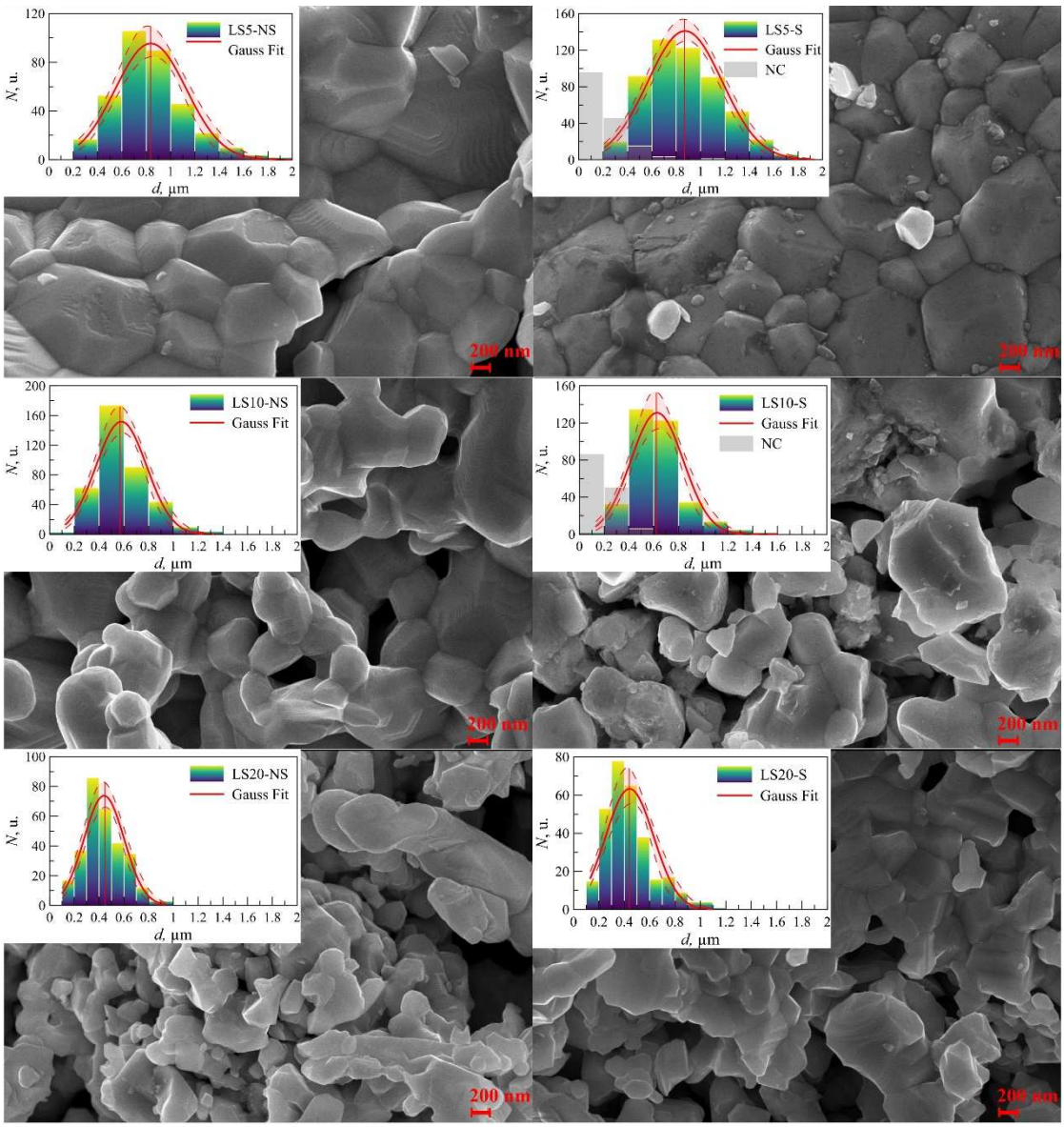

Fig. 2. SEM pictures for all samples and histograms with agglomerate size distribution with Gauss fitting.

Fig.3.

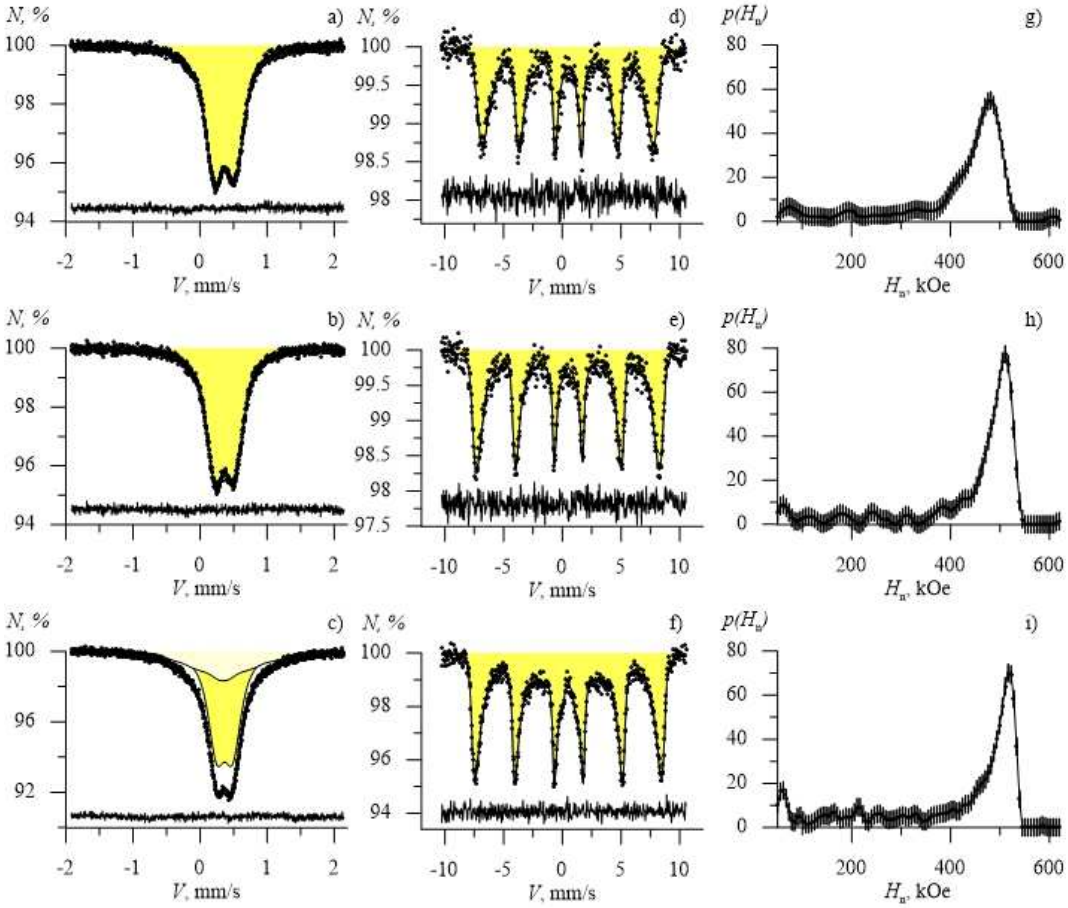

Fig. 3.[57]Fe Mössbauer spectra of LSM-NS measured at room temperature and 80 K (with distributions) (a,d,g – LS5-NS, b,e,h – LS10-NS and c,f,i – LS20-NS respectively).

Fig.4.

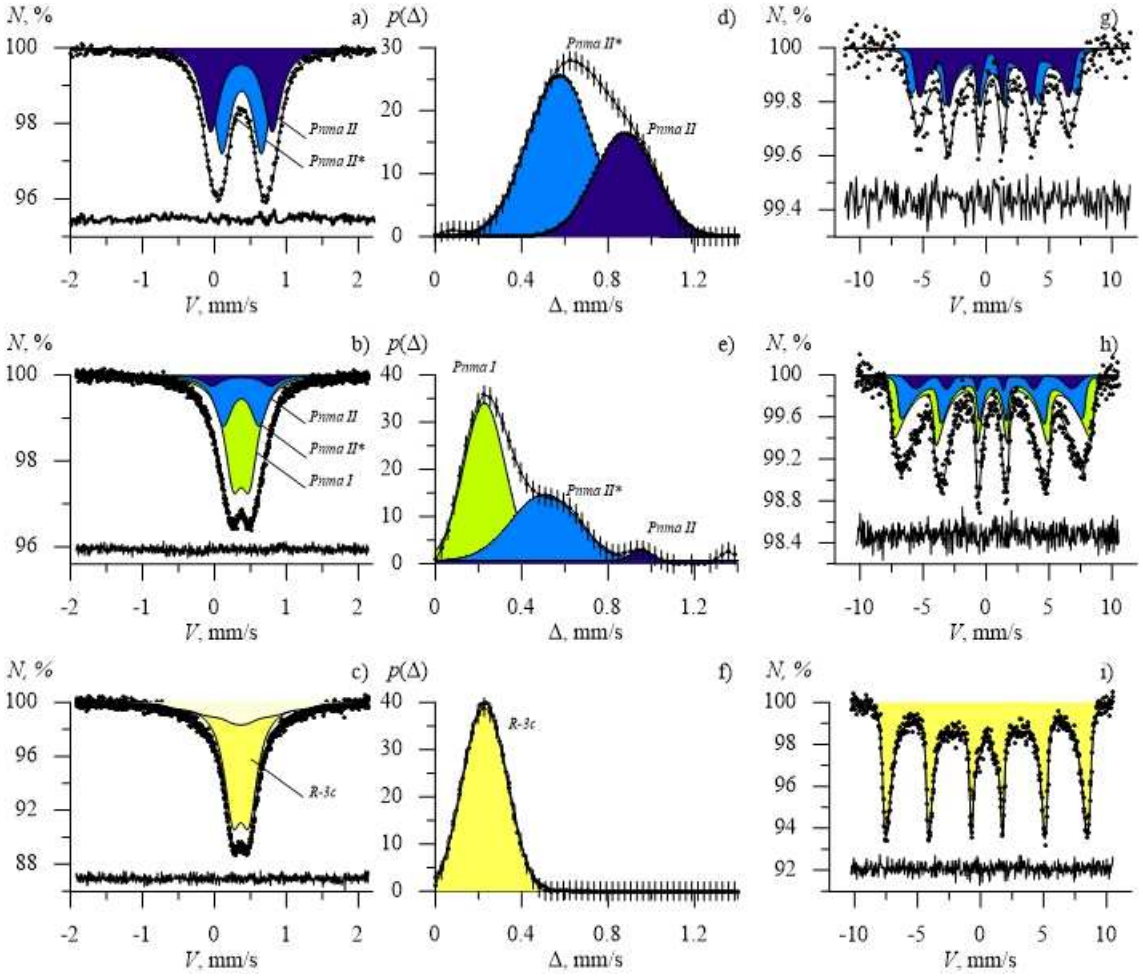

Fig. 4. ^{57}Fe Mössbauer spectra and distributions of LSM-S measured at room temperature and 80 K (a,d,g – LS5-S, b,e,h – LS10-S and c,f,i – LS20-S respectively).

Fig.5.

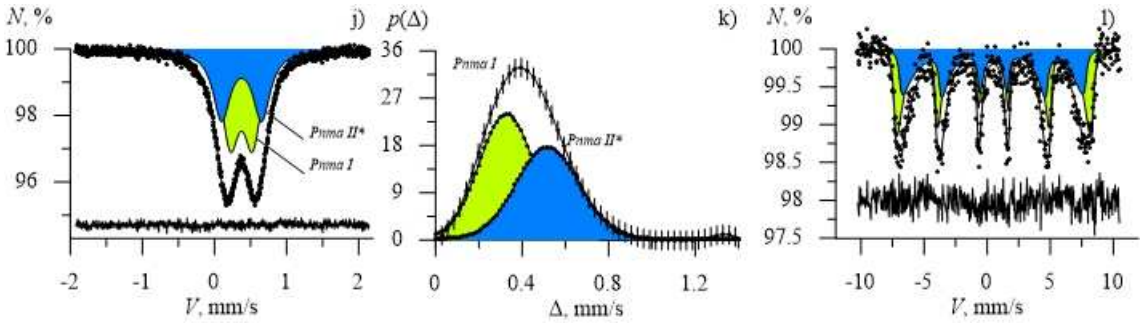

Fig. 5. ^{57}Fe Mössbauer spectra and distribution of LS5* measured at room temperature (j,k) and 80 K (l).

Fig.6.

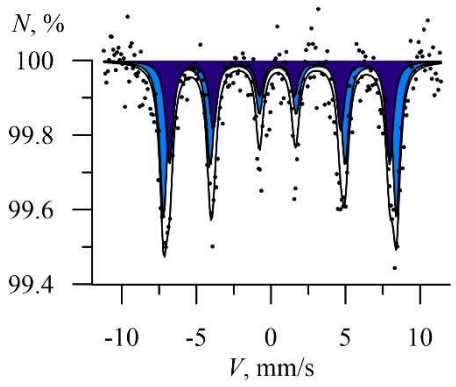

Fig. 6. ^{57}Fe Mössbauer spectra of LS5-S measured at 5 K.

Fig.7.

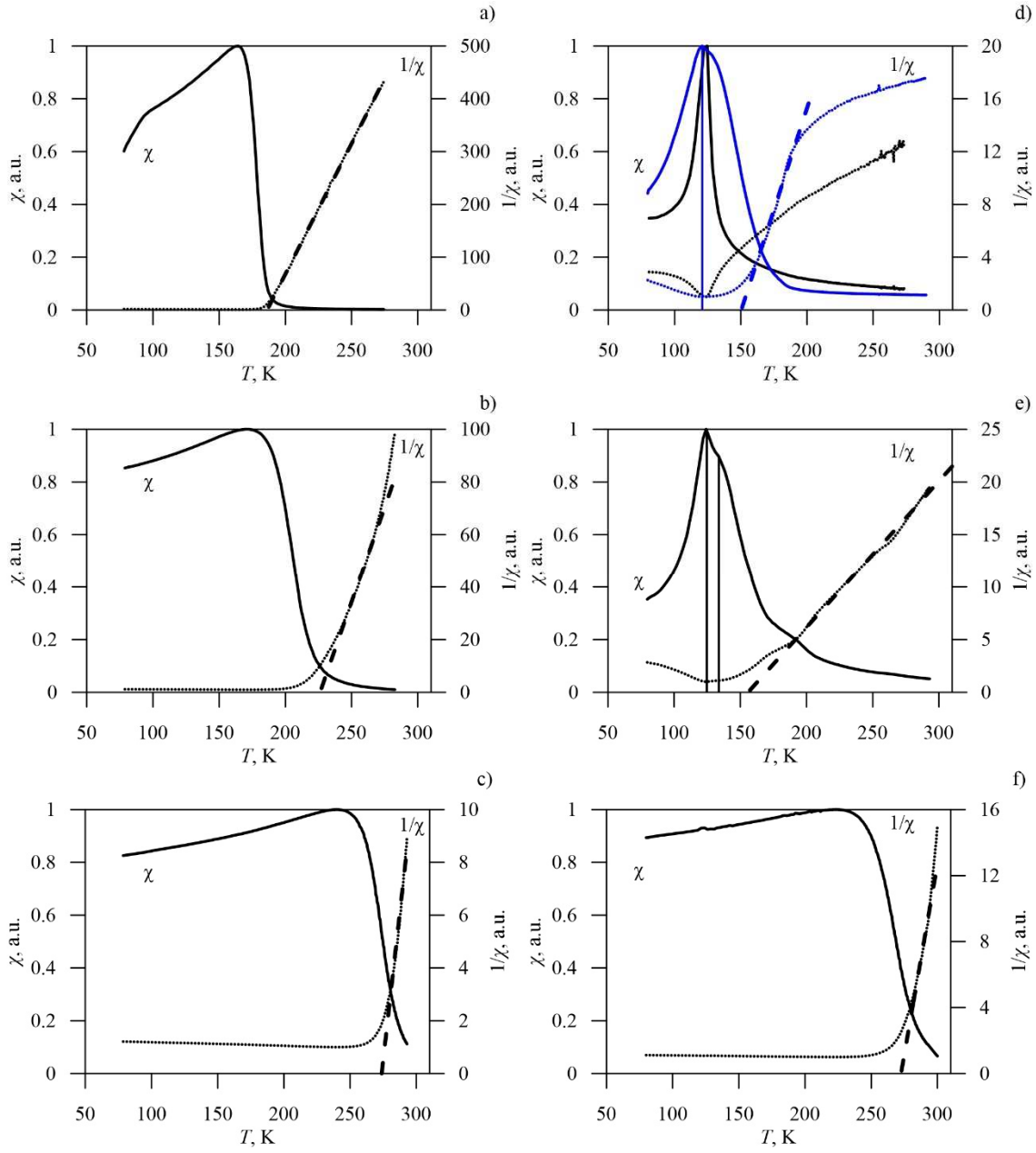

Fig.7. Temperature dependences of the direct and inverse susceptibility for the samples a) LS5-NS, b) LS10-NS, c) LS20-NS, d) LS5-S and LS5*(blue), e) LS10-S, f) LS20-S.

Fig.8.

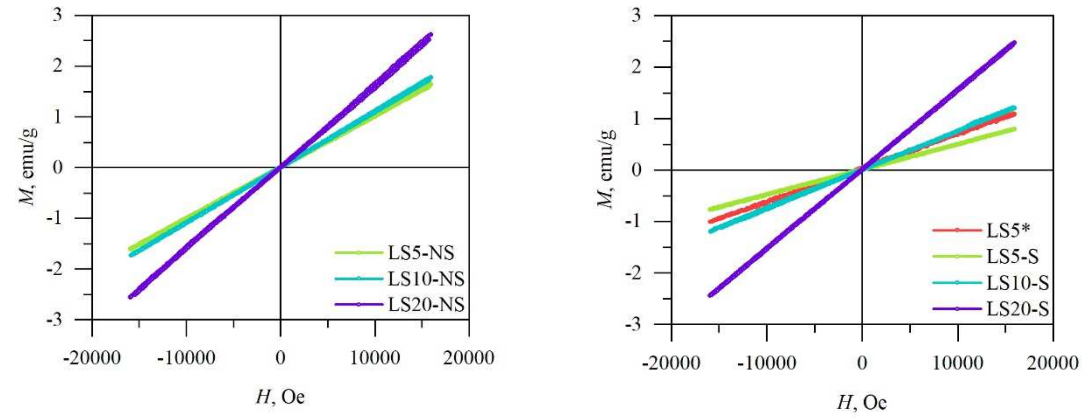

a) Loops 400K

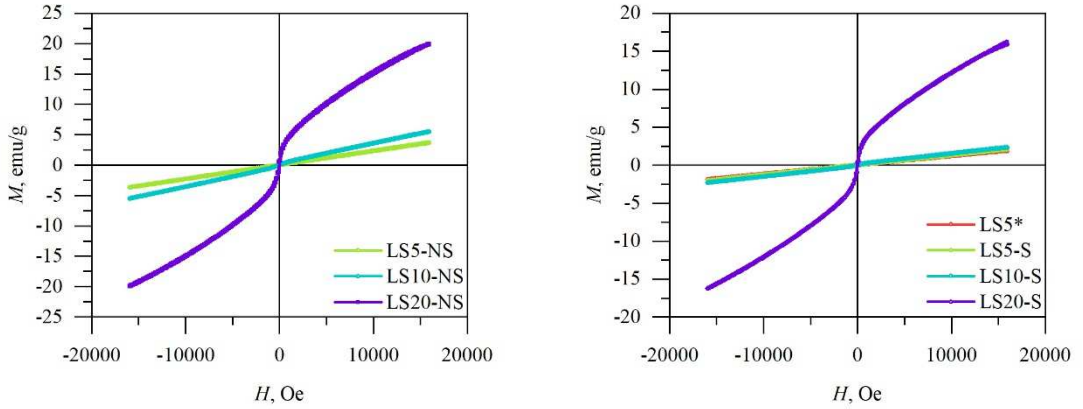

b) Loops RT

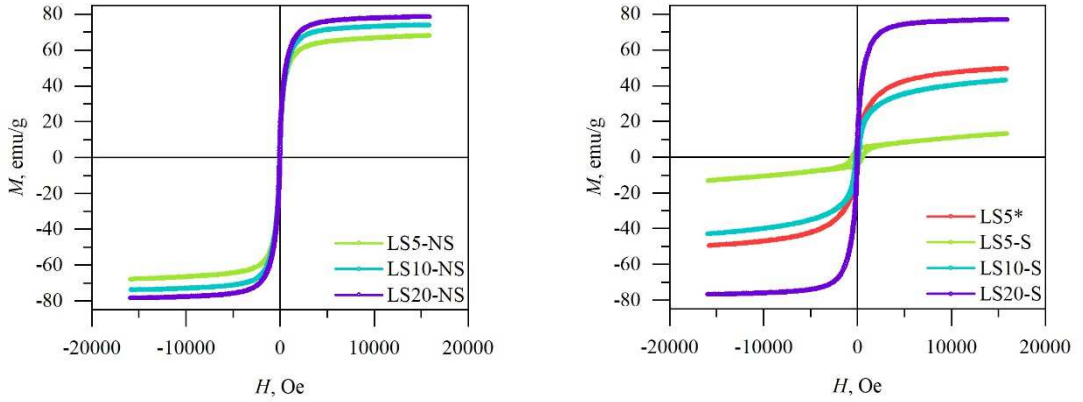

c) Loops 100K

Fig.8. Hysteresis loops obtained at 400 (a), RT(b), 100 K(c) for all samples.

Fig. 9.

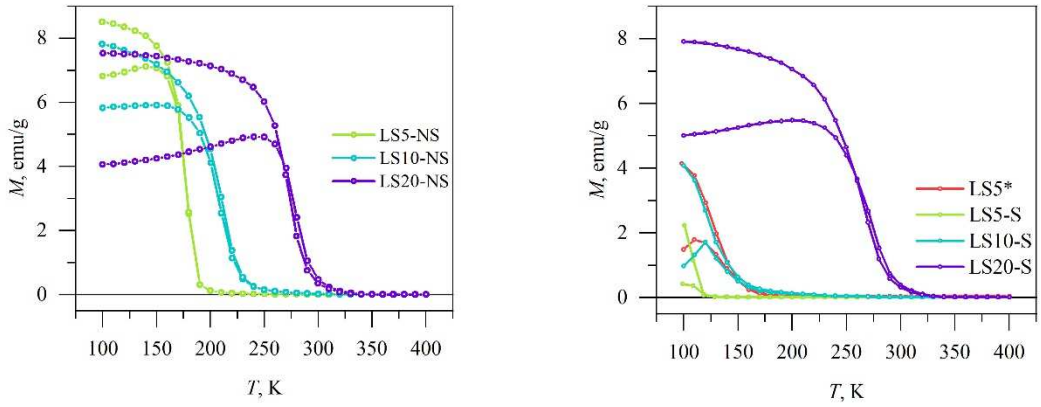

ZFC-FC

Fig. 9. The temperature dependence of the magnetization (ZFC/FC measurements) for all samples.

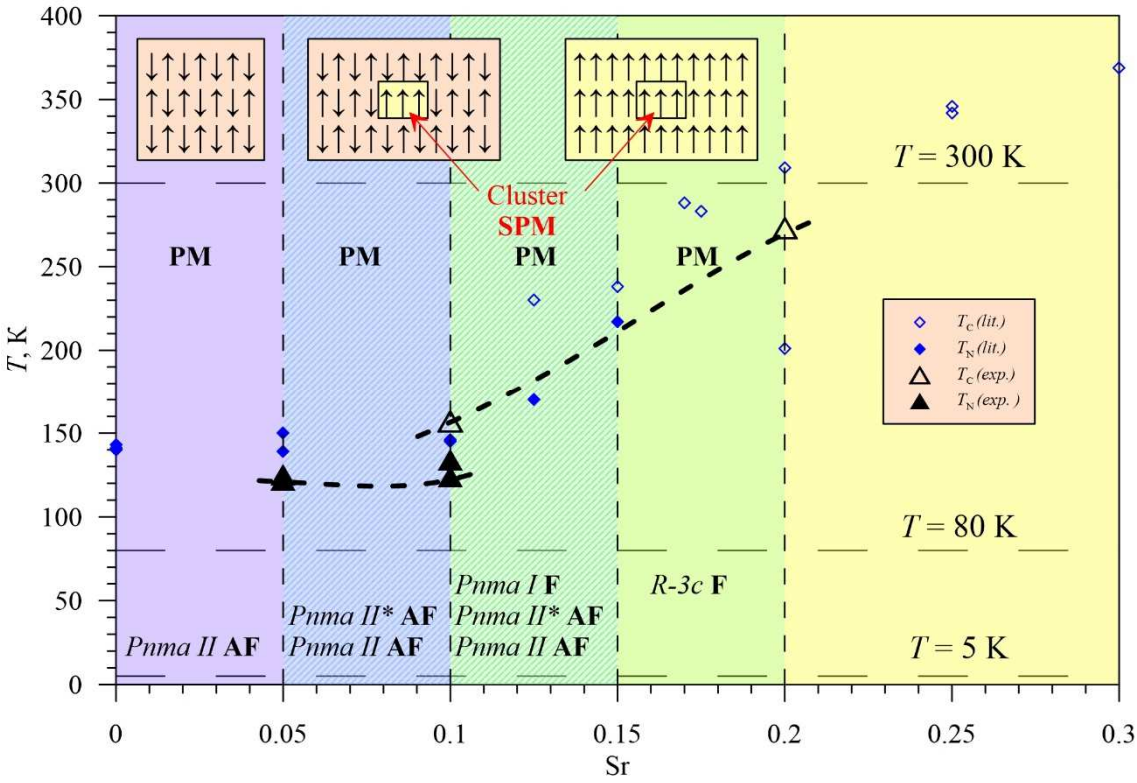

Fig. 10. Magnetic phase diagram for $La_{1-x}Sr_xMnO_3$ (x = 0.05, 0.10, 0.20).